Journal of Physics D:
Applied Physics

PURPOSE-LED
PUBLISHING™

The effect of rapid thermal annealing on 1.55 μm InAs/InP quantum dots

To cite this article: Calum Dear *et al* 2025 *J. Phys. D: Appl. Phys.* **58** 125104

OPEN ACCESS
IOP Publishing

Journal of Physics D: Applied Physics

J. Phys. D: Appl. Phys. **58** (2025) 125104 (9pp)

https://doi.org/10.1088/1361-6463/adabf1

The effect of rapid thermal annealing on 1.55 μm InAs/InP quantum dots

Calum Dear[1], Jae-Seong Park[1], Hui Jia[1], Khalil El Hajraoui[2,3], Jiajing Yuan[1], Yangqian Wang[1], Yaonan Hou[4,5], Huiwen Deng[1], Qiang Li[6], Quentin M Ramasse[2,7], Alwyn Seeds[1], Mingchu Tang[1,*] and Huiyun Liu[1]

[1] Department of Electronic and Electrical Engineering, University College London, London WC1 E7J, United Kingdom
[2] SuperSTEM, SciTech Daresbury Science and Innovation Campus, Block J, Keckwick Lane, Daresbury WA4 4AD, United Kingdom
[3] York NanoCentre & Department of Physics, University of York, York YO10 5DD, United Kingdom
[4] Department of Electronic and Electrical Engineering, Bay Campus, Swansea University, Swansea SA1 8EN, United Kingdom
[5] Centre for Integrative Semiconductor Materials (CISM), Bay Campus, Swansea University, Swansea SA1 8EN, United Kingdom
[6] School of Physics and Astronomy, Cardiff University, Cardiff CF24 3AA, United Kingdom
[7] School of Chemical and Process Engineering and School of Physics and Astronomy, University of Leeds, Leeds LS2 9JT, United Kingdom

E-mail: hui.jia@ucl.ac.uk and mingchu.tang@ucl.ac.uk

Received 4 October 2024, revised 2 January 2025
Accepted for publication 20 January 2025
Published 29 January 2025

Abstract

Rapid thermal annealing (RTA) can be used as a post-growth method to adjust the optical properties of III–V materials. This work investigates the efficacy of applying cyclic RTA to 1.55 μm multi-layer InAs/InAlGaAs quantum dots (QDs) grown on (001) InP substrate by molecular beam epitaxy. Samples cyclically-annealed at 600 °C retain most of their as-grown optical, structural, and compositional characteristics whilst exhibiting a 4.6-fold increase in peak PL intensity. This strategy was successfully implemented in broad-area devices with improved slope efficiency and output power, demonstrating cyclic RTA as an effective method in enhancing high-performance 1.55 μm QD lasers on InP (001) substrates.

Supplementary material for this article is available online

Keywords: quantum dots, rapid thermal annealing, molecular beam epitaxy

1. Introduction

The three-dimensional confinement in self-assembled quantum-dot (QD) materials can be harnessed to produce lasers with superior temperature stability, low threshold current density and defect tolerance [1–4]. Recently, QD-based laser devices on the InAs/GaAs platforms have demonstrated tremendous progress for O-band applications [5–8]. For contemporary long-haul applications, C-band emission can be realised by utilising the low lattice mismatch between InAs and InP (3.2%) to nucleate larger nanostructures [9, 10]. However, the low-strain InAs/InP interface gives rise to complex surface interactions, causing InAs nanostructures on InP (001) to nucleate as anisotropically-elongated quantum dashes at low deposition thicknesses [9, 11, 12], thereby delaying progress compared to the InAs/GaAs platform.

---

[*] Author to whom any correspondence should be addressed.

To leverage the discrete carrier localisation properties of QDs, a substantial number of growth techniques have been investigated to preferentially nucleate dot-like nanostructure morphologies over quantum dashes. These techniques include employing As_2 flux [13], an optimised V/III beam equivalent pressure (BEP) ratio [14], GaAs and InGaAs pre-layers [15, 16], and various buffer layers on which the QDs are deposited [17, 18]. Employing an InAlGaAs buffer has been demonstrated as particularly effective in attenuating the migration length of In adatoms and enhancing QD nucleation due to its surface roughness [14]. Whilst C-band emission with respectable linewidths around 40 meV at room temperature (RT) was recently reported [19], the buffer layers' rough surfaces are typically attained at sub-optimal growth temperatures. This could promote the formation of crystalline point defects (PDs) around the QDs [15, 20], effectively degrading the optical properties in terms of reducing the ratio of radiative transitions, thus decreasing the gain saturation of lasing devices.

An improvement in the optical quality of QD materials can be achieved by means of post-growth rapid thermal annealing (RTA), which is attributed to two distinct mechanisms. The first is the removal of PDs and, therefore, an increase in radiative transitions [21, 22]. The second follows as a product of thermally-induced intermixing, whereby QDs become alloyed and increase in size with an enhanced carrier population and quantum yield [23, 24]. Whilst intermixing at higher temperatures in the InAs/GaAs system improves QD homogeneity by means of $In_xGa_{1-x}As$ alloying of the dots, resulting in narrower full-width at half-maximum (FWHM) in photoluminescence (PL) spectrum [23], RTA treatment of QDs with Al-containing buffers results in the deterioration of the QDs' electronic shells due to diffusion of Al into the dots, thereby broadening the PL linewidth [25]. Furthermore, thermal intermixing diminishes material contrast between the QDs and surrounding buffer layer [26], affecting quantum confinement [27], and, in cases of extensive intermixing, destroying the QDs [28].

However, at the intermixing-threshold temperature, where the thermal energy has not surpassed the cohesive energy of the crystal, previous works have observed an improvement in optical quality [27, 29] and enhanced laser characteristics in threshold current density and ground-state modulation [29–31]. The cohesive energies of InAs, GaAs, and AlAs binaries, which are defined as the difference between isolated atomic energy and the total crystal energy, have been calculated in good agreement with experimental results as 5.94, 6.37, 7.49 eV, respectively [32–34]. Therefore, the differing binary cohesive energies potentially present complex thermally-induced intermixing behaviours in an InAlGaAs quaternary. Yet, the extent of RTA's capabilities on both the improvement to optical properties and performance of InAlGaAs-buffered InAs/InP QD lasers is scarcely explored.

In this work, we investigate the effect of cyclic (repeated) RTA at temperatures between 600 and 650 °C on InAs/InP (001) QDs with an InAlGaAs buffer. This work demonstrates that cyclically-annealing QDs at the intermixing-threshold temperature improves optical properties, yielding a 4.6-fold increase in peak PL intensity with negligible degradation of key optical characteristics such as wavelength and FWHM. Furthermore, scanning transmission electron microscopy (STEM) and electron energy loss spectroscopy (EELS) images of the reference and annealed samples were investigated to determine the structural and compositional impact of cyclic RTA, respectively. By employing cyclic RTA in Fabry–Pérot (FP) broad-area (BA) laser structures, we report an increase in slope efficiency and maximum output power.

2. Experimental setup and methodology

The epitaxial structure in this study, illustrated in figure 1(a), was grown on an n-type InP (001) substrate using a Veeco GEN930 solid-source molecular beam epitaxy (MBE) system equipped with a valved arsenic cracker source. Prior to growth, the wafer was degassed at 400 °C for 1 hour in the preparation chamber, followed by a 1 min anneal at 500 °C in the growth chamber under As_2 overpressure to remove surface oxides. Immediately following thermal deoxidation, 500 nm $In_{0.524}Al_{0.476}As$ and 100 nm $In_{0.528}Al_{0.238}Ga_{0.234}As$ buffer layers were grown (henceforth referred to as InAlAs and InAlGaAs, respectively). All layers, excluding the InAs QDs, were lattice-matched to InP. The first 50 nm and following 450 nm of InAlAs were grown at 485 °C and 510 °C, respectively, to promote a high-quality interface between the InAlAs and InP. Unless stated otherwise, all further InAlAs and InAlGaAs buffers were grown at 510 °C and 500 °C, respectively.

For the QDs, 5.5 MLs of InAs was deposited in As_2 mode on InAlGaAs buffer at 485 °C with a growth rate of $0.42\ \mathrm{ML\ s^{-1}}$ and a V/III BEP ratio of 18 [35], followed by a 10 s growth interruption under As_2 pressure to stabilise QD formation and reduce island size dispersion [36]. A partial cap of 4 nm of InAlGaAs was deposited on top of the QDs at QD growth temperature, followed by an indium flush at 540 °C for 1 min under As_2 pressure [35, 37], followed by a 36 nm InAlGaAs spacer layer. This was repeated so that five layers of QDs were separated by 40 nm spacer layers of InAlGaAs. After the QD layers, a total 100 nm of InAlGaAs was deposited. The growth was completed by 100 nm of InAlAs and 100 nm of InAlGaAs.

For post-growth RTA, the wafers were coated with 200 nm of SiO_2 using plasma-enhanced chemical vapour deposition to protect the samples. $7 \times 7\ \mathrm{mm^2}$ dies were cut and annealed in a Solaris 150 RTA oven in an N_2 environment. Each die was annealed multiple times at fixed temperatures between 600 °C–650 °C for 60 s per cycle, where the samples were removed between each cycle for PL measurements. For consistency, all PL measurements, including the unannealed reference, were acquired with the SiO_2 layer applied.

For PL measurements, the samples were excited by a 635 nm continuous-wave laser with an excitation power density of $430\ \mathrm{W\ cm^{-2}}$. The spectra were collected by a wavelength-extended InGaAs detector with a cut-off wavelength of 2 μm. All PL measurements were performed at

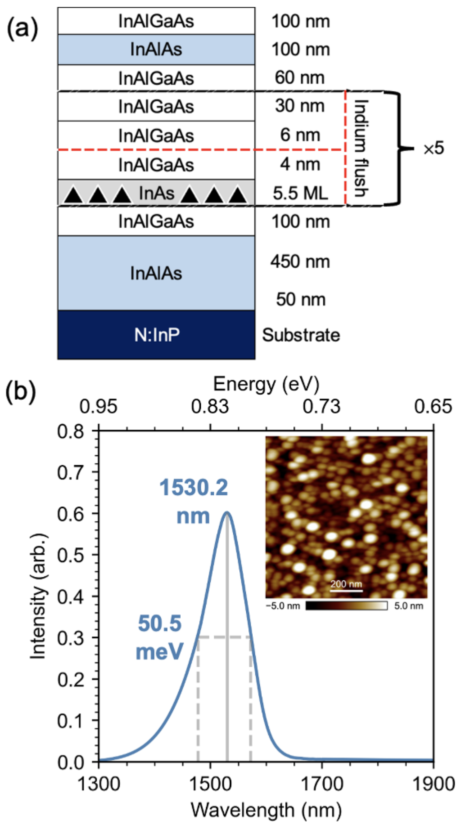

Figure 1. (a) Diagram of the five-QD layer structure investigated. (b) Room-temperature PL spectrum of the five-layer structure. The inset in (b) displays a 1 × 1 μm^2 AFM image of an uncapped ensemble of 5.5 ML QDs without a partial cap or indium flush, with otherwise nominally identical growth conditions to the QDs from the five-layer structure.

RT. Cross-sectional high-angle annular dark field (HAADF) images and EELS maps of focused-ion-beam-prepared lamellae (using an identical methodology to that described in [38]), performed in a STEM operated at 100 kV, were obtained for structural and chemical characterisations.

Additionally, a separate seven-layer laser structure was grown and fabricated into electrically-pumped FP BA devices. The structure was similar to the five-layer structure up until the upper InAlAs cladding. Both doped InAlGaAs buffer layers and InAlAs claddings were each 200 nm thick, where p- and n-dopants were Be and Si, respectively. The QDs were nominally identical to the five-layer structure, apart from spacer layers totalling to 30 nm. The QD region was separated from the doped layers with 30 nm of undoped InAlGaAs. After the upper InAlAs cladding, 40 nm, 1700 nm, and 200 nm of p-doped InAlAs, InP, and InGaAs contact layer were deposited via metal organic chemical vapour deposition.

3. Effects of cyclic RTA on QD characteristics

Figure 1(b) presents the PL spectrum from as-grown QDs, exhibiting peak emission at 1530.2 nm and a FWHM of 50.5 meV. The inset of figure 1(b) displays a 1 × 1 μm^2 atomic force microscopy (AFM) image of an uncapped QD ensemble of 5.5 ML QDs without a partial cap or indium flush with otherwise nominally identical growth conditions to the five-layer structure investigated. The QD density in this image is approximately 4×10^{10} cm^{-2}.

To investigate the effect of cyclic annealing on the optical characteristics of the QDs, the PL spectra of the cyclically-annealed samples at 600, 625, and 650 °C were acquired, where ‘ref.’ refers to each sample’s unannealed reference measurement, as presented in figures 2(a)–(c). A direct observation of figures 2(a)–(c) concludes that 600 °C annealing results in no intermixing-induced emission wavelength shift while significantly improving PL intensity with increased number of annealing cycles. On the other hand, 625 and 650 °C annealing led to wavelength shifts and PL intensity fluctuations to various extents.

Whilst not presented in these results, a separate study was conducted to investigate the effect of cyclic versus continuous annealing for various hold times. Samples which were annealed continuously at 600 °C exhibited an increase in PL intensity comparable to what was observed for the ×1 cycle in figure 2(a), irrespective of annealing time. This behaviour suggests the cyclic nature of RTA temperature ramping assists in increasing defect diffusion mobilities, similar to methods reported on integration of III–V buffer layers on Si via MBE [39].

Presenting the optical characteristics in more detail, figures 2(d)–(f) summarises the shift, relative to each respective unannealed reference measurement, in peak emission wavelength, FWHM, and peak signal intensity as a function of annealing cycles for each annealing temperature, respectively. The error is represented as a 95% confidence interval for each characteristic, calculated from the standard error of the mean obtained via a 2D spectral scan of each 7 × 7 mm^2 die between each cycle.

The shift in wavelengths plotted in figure 2(d) displays linear blue-shifts of −(2.3 ± 0.6), −(15.4 ± 0.8), and −(81.2 ± 4.4) nm/cycle for the 600, 625, and 650 °C annealing temperatures, respectively. The 650 °C blue-shift value is calculated from the linear regime in the first two annealing cycles. By the fifth anneal, a total blue-shift of 13.3, 75.5, and 226.6 nm was observed for the 600, 625, and 650 °C annealing temperatures, respectively. Evaluating on blue-shift, it appears that minor levels of intermixing occurred for the 600 °C sample, whereas the 625 and 650 °C samples indicated increased levels of intermixing. This is further confirmed in the STEM-EELS analysis, to be presented shortly. Whilst thermal intermixing-induced blue-shift is commonly reported by means of single-cycle RTA [40–42], less so is the blue-shift behaviour under cyclic conditions as demonstrated here.

By the fifth cycle, the total observed FWHM broadening in figure 2(e) was 1.1, 14.4, and 13.3 meV for the 600, 625, and 650 °C annealing temperatures, respectively. The samples annealed at 600 °C and 625 °C exhibit a linear relation of broadening in linewidth. This behaviour can be described by the continual intermixing and lowering of confinement quality due to the reduced interface contrast between the QDs and

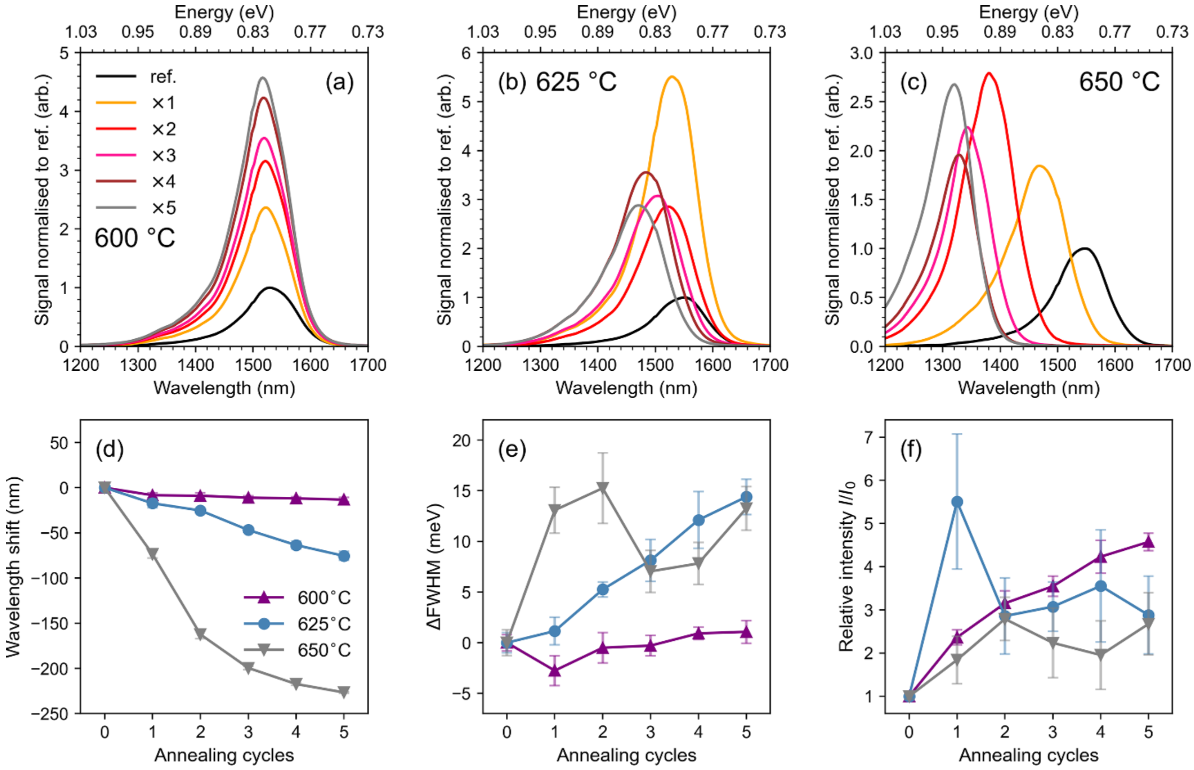

Figure 2. PL spectra at RT from the five-layer structure wafer, each individually annealed five times at respective fixed temperatures of (a) 600, (b) 625, and (c) 650 °C for 60 s each cycle, including each respective unannealed reference. Plots of shifts in (d) wavelength, (e) FWHM, and (f) relative signal intensity as a function of annealing cycles, extracted from the spectra shown in (a)–(c). Each sample's annealed characteristic is normalised its respective unannealed reference measurement.

surrounding spacer layer matrix [26, 27], which is also evidenced in the STEM characterisation discussed below. The cyclically-annealed sample at 650 °C, however, first exhibits a large broadening in PL linewidth, followed by a temporary reduction by the third annealing cycle. This behaviour is discussed further in relevance to figure 3(c).

In figure 2(f), by the fifth anneal, the increase in peak PL intensities for the samples annealed at 600, 625, and 650 °C were 4.6, 2.9 and 2.7 ×, respectively, compared to their respective reference peak intensities. The sample annealed at 625 °C unexpectedly exhibited a 5.5 × increase in peak intensity in the first annealing cycle compared to its unannealed reference. Disregarding the increase in intensity from the sample annealed once at 625 °C due to its high margin of error, the 600 °C-annealed sample consistently remained the highest increase in intensity across all annealing cycles.

To determine the impact of cyclic RTA on the structural properties of QDs, cross-sectional high-resolution HAADF images of the QD regions of an unannealed reference structure and samples annealed for five cycles at 600 °C and 650 °C, displayed in figures 3(a)–(c), were investigated. It should be noted that features unrelated to the cyclic annealing process are evident in every HAADF image resulting from the indium flush during growth, such as (001) facets atop larger QDs and dark, In-depleted regions connecting the top corners of each QD [37, 43].

Visually inspecting the structural characteristics of the reference sample and the five-times 600 °C annealed sample (figures 3(a) and (b)) using STEM-HAADF, both appear to exhibit good contrast and therefore a clear separation of the matrix material and QDs [44] since HAADF image intensity scales to a good approximation with the average atomic number Z as Z^n ($n = 1.4$–1.8) [45]. However, careful inspection of the high-magnification image of figure 3(b) reveals a subtle reduction in contrast across the base of the QD. This observation suggests a compositional homogenisation across the interface between the QD and the underlying buffer, with In and Ga interdiffusion through annealing leading to a loss of interfacial contrast sharpness. This is thought to be due to a strain-enhanced lower intermixing activation energy at the highly-strained QD base [28], which corroborates with evidence in the PL that a minor level of intermixing had occurred. The high strain level between the matrix and the QD [46] is also confirmed from geometrical phase analysis (GPA) [47] carried out on the high resolution HAADF images and revealing a nearly 4.5% tensile (positive) strain level within the QD compared to the matrix reference in the unannealed sample, dropping only slightly to 3% after five cycles at 600 °C (see supplementary information, figure S2 for more details on the GPA analysis).

For the five-times 650 °C annealed sample in figure 3(c), a more substantial loss in contrast across the interface with the buffer is observed, along with a reduction in measured strain by GPA (only 1% in the QD compared to the neighbouring matrix reference, see figure S2), evidence of further compositional homogenisation. An increase in dot size laterally is also

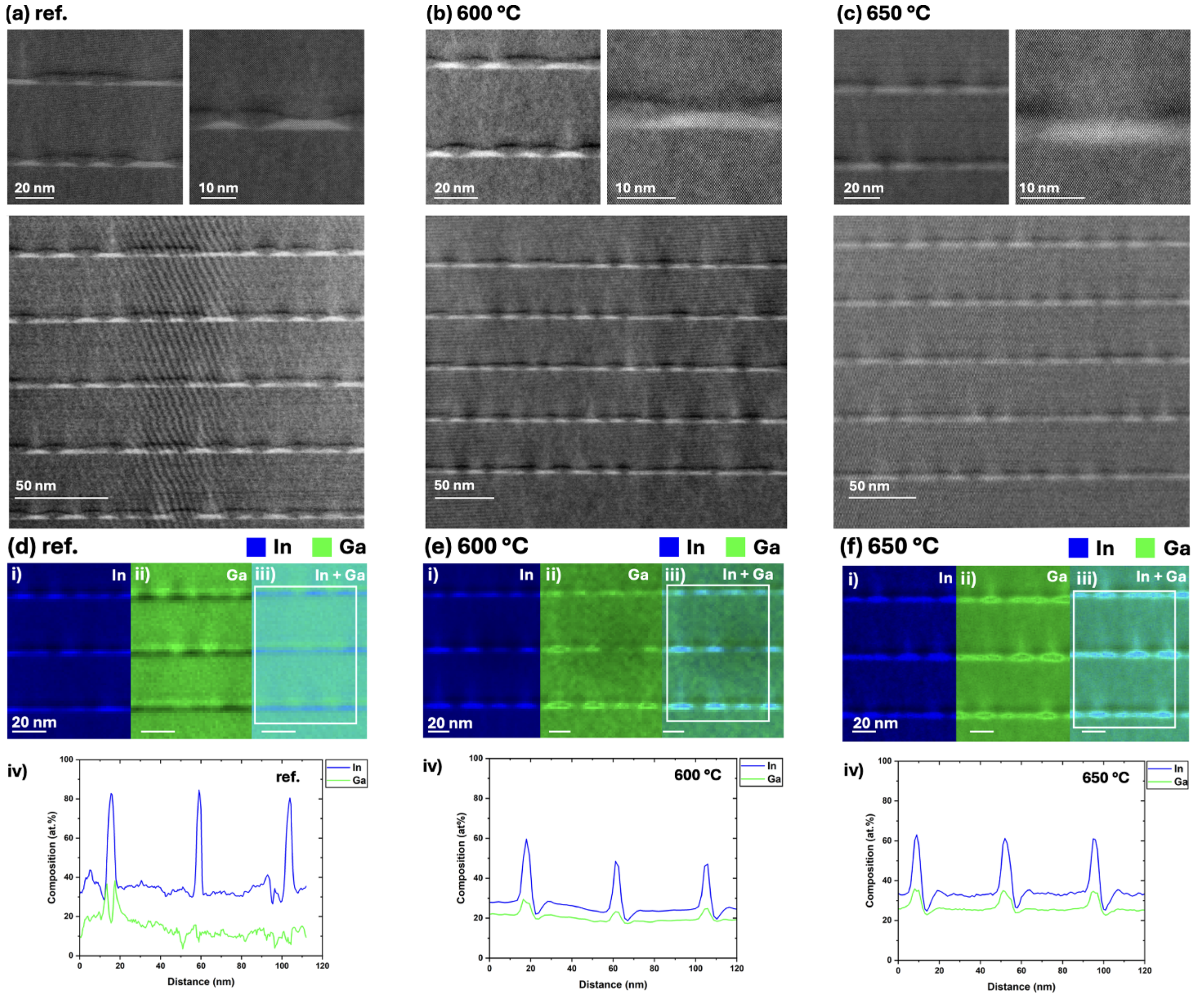

Figure 3. HAADF images at various magnifications of (a) an as-grown reference sample, and samples after five cycles of (b) 600 °C and (c) 650 °C RTA. Individual and composite EELS images detailing the In (blue channel) and Ga (green channel) compositions with the relative compositional profiles along the region of interest highlighted by a white box in the composite maps of (d) the as-grown, (e) 600 °C, and (f) 650 °C samples. Individual EELS maps of the three elements and corresponding HAADF images are provided for completeness in the supporting information.

clear, with individual QD (111) facets almost merging with neighbouring QDs. Moreover, the smaller, fully-capped QDs often observed in the unannealed sample appear to have disappeared. The loss of smaller QDs in the 650 °C-annealed sample serves as an explanation for the behaviour seen in figures 2(d)–(f). By the third and fourth annealing cycles, a reduction in linewidth and peak intensity is observed, potentially coinciding with the destruction of the smaller QD population and temporarily improving uniformity and reducing the dot population (relative to the second annealing cycle), respectively.

The nano-scale chemical composition of the QDs and surrounding InAlGaAs buffer was investigated using EELS in figures 3(d)–(f), which shows the relative distribution of In and Ga of the reference, and five-times 600 °C and 650 °C annealed samples. In the reference unannealed sample, the QDs show intense In contrast, confined laterally to well defined dimensions with sharp (111) facets (with no Ga or Al, see figures 3(d–ii), (iv) and S4 for the three corresponding maps). In the five-times 600 °C-annealed sample, some QDs already exhibit evidence of lateral intermixing between Ga and In (with the Al relative distribution remaining mostly unchanged: maps for Al are presented in supplementary information for completeness), see figure 3(e-iii) and (iv) [28]: the In distribution appears more continuous along the QD layers, and the relative In intensity in the matrix appears higher, confirming the intermixing process. This trend is even more pronounced for the 650 °C-annealed sample, where the In signal is far more intense in the matrix, and continuous (but at a reduced level along the QD layer), indicating high levels of intermixing, as shown in figure 3(f) and the compositional line profile in figure 3(f–iv).

At both annealing temperatures, the Al distribution remains comparable to that of the reference sample, likely due to the strong Al bonding energy and corresponding short interdiffusion length at these temperatures [48, 49]. This results in In–Ga intermixing only. Besides, Al incorporation into the QDs typically leads to a deterioration of their electronic shells, which causes a reduction in PL intensity [25] not observed in these results.

Although the 600 °C cyclic annealing cannot precisely be defined as intermixing-threshold, a 4.6-fold increase in peak PL intensity is observed with negligible degradation to other key characteristics. The increase in intensity demonstrated here is inconsistent with the levels of intermixing-induced blue-shift reported in previous works focused on single-cycle RTA [23, 27, 40–42, 50]. Contrasting this with the similarity in structure and composition with the unannealed reference in the HAADF and EELS images, it is improbable that the increase in intensity originates from an increase in dot size or change in composition alone. Therefore, the likely mechanism in intensity increase is the improvement in optical quality by means of increase in radiative transitions, typically facilitated by the removal of PDs [27, 29].

4. Effects of cyclic RTA on laser characteristics

In the following, we have investigated the effect of 600 °C cyclic RTA on the static performance of FP BA devices with a seven-QD layer structure to enhance lasing gain. From the laser structure, a reference die was left unannealed while another was annealed at 600 °C for five cycles with 20 s per cycle. A separate study (not shown here) was conducted on a sample identical to figure 1(a) for optimal annealing hold time to minimise blue-shift. It was determined that a 20 s hold time yielded a lower shift in wavelength and linewidth ($-$ 7.0 nm and + 0.39 meV, respectively) while exhibiting a 4.1-fold increase in peak PL intensity after five cycles.

Following annealing, the SiO_2 layers were removed by standard buffered oxide etch. Thereafter, BA devices with a 50 μm cavity width were fabricated from the structures using conventional photolithography and wet etching processes. P-type and n-type electrodes of Ti/Au and Ni/AuGe/Ni/Au were deposited for the top and bottom contacts, respectively, followed by a 1 min anneal at 380 °C to form an ohmic contact. No wafer thinning or facet coatings were applied. The laser bars were cleaved into cavity lengths of 500 and 750 μm.

Figure 4(a) presents the typical RT light–current (L–I) curves of the BA devices under pulsed operation with a pulse width of 1 μs and 1% duty cycle. Comparing the reference and annealed devices, an increase in slope efficiency was observed from 0.053 to 0.088 W A^{-1} and from 0.052 to 0.075 W A^{-1} for the 500 and 750 μm cavity lengths, respectively. Additionally, an increased measured maximum output power was achieved between the reference and annealed devices from 42.2 to 71.3 mW for the 500 μm cavity lengths and 51.9 to 74.3 mW for the 750 μm cavity lengths, respectively.

However, between the reference and annealed 500 μm devices, the threshold current increased from 271 mA to 366 mA, corresponding to a threshold current density of 1085 A cm^{-2} and 1464 A cm^{-2}, or 155 A cm^{-2} and 209 A cm^{-2} per QD layer, respectively. Similar behaviour is observed for the 750 μm cavity lengths. The increase in threshold current may result from Ga-outgassing during RTA between an InGaAs contact layer and the porous SiO_2 capping layer [51], degrading the ohmic contact. This could be avoided with a GaAs proximity cap method [29]. Additionally, thermally-assisted diffusion of beryllium dopants into the QDs may have further increased the threshold current [52], where adjusting dopant concentrations or the use of a dopant-diffusion barrier layer could limit this behaviour.

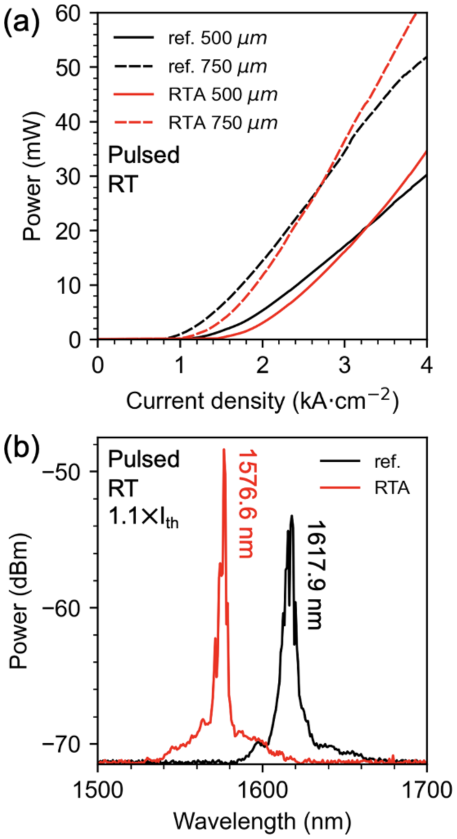

Figure 4. (a) L–I characteristics of 50 μm wide BA devices with 600 °C five-times cyclic RTA and an unannealed reference at RT under pulsed conditions using a 1 μs pulse and 1% duty cycle. (b) RT lasing spectrum at 1.1 × Ith for the unannealed and five-times annealed 50 × 500 μm^2 BA devices.

Figure 4(b) displays the RT lasing spectra at 1.1 × Ith under pulsed conditions for the 500 μm reference and annealed devices, measuring peak wavelengths of 1617.9 and 1576.6 nm, respectively. Noted that the difference in peak lasing wavelength of the seven-layer reference laser and the peak wavelength of the five-layer as-grown PL spectrum (figure 1(b)) can be attributed to an increase in average dot size due to enhanced strain coupling from the increased number of layers in the seven-layer structure [53, 54]. It is proposed that a five-layer laser structure can achieve the desired C-band emission as shown in the reference PL measurements. Furthermore, the peak lasing wavelength of the annealed devices exhibits a shift of approximately 41 nm compared to the reference devices. This increased blue shift, relative to the PL observations for the five-layer structure, could be attributed to the enhanced strain in the seven-layer structure. The intermixing threshold is likely lowered by the additional strain, facilitating strain-enhanced intermixing [28].

5. Conclusion

A 4.6-fold increase in peak PL intensity has been attained in a five-layer InAs/InAlGaAs/InP (001) QD structure by cyclically-annealing for five cycles using RTA at 600 °C. The cyclic nature of post-growth RTA has been revealed to be an effective method to improve PL intensity and optical activity of a QD structure with minor effects of thermal-intermixing observed in optical, structural, and compositional characteristics. This evidences that an increase in intensity was unlikely due to the influence of intermixing. Moreover, cyclic RTA has been demonstrated as an applicable step in the laser fabrication process to improve slope efficiency and maximum output power. These results demonstrate a fast and cost-effective solution to improve optical quality, enabling high-performance III–V photonic devices.

6. Methods

The electron microscopy characterisation was performed using a probe-corrected Nion UltraSTEM microscope operating at 100 kV. The microscope is equipped with a cold field emission electron source with a nominal energy spread of around 0.3 eV. The electron optics were adjusted to a convergence half-angle of 30 mrad, a beam current of ∼40 pA and a probe size of ∼1 Å. HAADF (90–190 mrad angular range) images were acquired as series to eliminate stage drift and scanning distortions using non-rigid registration methods [55]. The EEL spectrum images (SIs) were acquired with the zero-loss peak with an energy dispersion of 1.39 eV/channel to allow for precise energy calibration on a Gatan Enfina spectrometer retro-fitted with a Quantum Detectors Merlin EELS hybrid-pixel camera. The SIs were subsequently denoised using principal component analysis routine implemented in the multivariate statistical analysis plugin [56] in Digital Micrograph developed by Watanabe. Compositional quantification of the EELS data from the Al $L_{2,3}$, In $M_{4,5}$ and Ga $L_{2,3}$ EELS edges was carried out using the model-based approach implemented in Gatan Digital Micrograph, and originally developed by Verbeeck *et al* [57]. GPA was performed on HAADF image series (20 images aligned and averaged) to ensure a high signal-to-noise ratio [58].

Data availability statement

All data that support the findings of this study are included within the article (and any supplementary files).

Acknowledgment

This work was supported in part by Engineering and Physical Sciences Research Council (Grant Nos EP/V029681/1, EP/P006973/1, EP/S024441/1, EP/W021080/1, EP/V036432/1, EP/V029606/1, EP/Z532848/1, EP/T028475/1, EP/V036327/1, EP/V048732/1, and EP/X015300/1).

ORCID iDs

Calum Dear https://orcid.org/0000-0003-1356-705X
Jae-Seong Park https://orcid.org/0000-0002-6486-2342
Hui Jia https://orcid.org/0000-0002-8325-3948
Khalil El Hajraoui https://orcid.org/0000-0002-7627-6981
Huiyun Liu https://orcid.org/0000-0002-7654-8553

References

[1] Liu A Y, Srinivasan S, Norman J, Gossard A C and Bowers J E 2015 Quantum dot lasers for silicon photonics [Invited] *Photon. Res.* **3** B1–9

[2] Liu Z *et al* 2020 Origin of defect tolerance in InAs/GaAs quantum dot lasers grown on silicon *J. Light. Technol.* **38** 240–8

[3] Yan Z and Li Q 2024 Recent progress in epitaxial growth of dislocation tolerant and dislocation free III–V lasers on silicon *J. Phys. Appl. Phys.* **57** 213001

[4] Shang C, Wan Y, Selvidge J, Hughes E, Herrick R, Mukherjee K, Duan J, Grillot F, Chow W W and Bowers J E 2021 Perspectives on advances in quantum dot lasers and integration with Si photonic integrated circuits *ACS Photonics* **8** 2555–66

[5] Lv Z, Wang S, Wang S, Chai H, Meng L, Yang X and Yang T 2023 Ultra-high thermal stability InAs/GaAs quantum dot lasers grown on on-axis Si (001) with a record-high continuous-wave operating temperature of 150 °C *Opt. Express* **31** 24173

[6] Wang Y *et al* 2023 InAs/GaAs quantum-dot lasers grown on on-axis Si (001) without dislocation filter layers *Opt. Express* **31** 4862

[7] Yang J *et al* 2020 All-MBE grown InAs/GaAs quantum dot lasers with thin Ge buffer layer on Si substrates *J. Phys. Appl. Phys.* **54** 035103

[8] Chen S *et al* 2016 Electrically pumped continuous-wave III–V quantum dot lasers on silicon *Nat. Photon.* **10** 307–11

[9] Khan M Z M, Ng T K and Ooi B S 2014 Self-assembled InAs/InP quantum dots and quantum dashes: material structures and devices *Prog. Quantum Electron.* **38** 237–313

[10] Zhou Z, Ou X, Fang Y, Alkhazraji E, Xu R, Wan Y and Bowers J E 2023 Prospects and applications of on-chip lasers *eLight* **3** 1

[11] Ponchet A, Pedesseau L, Le Corre A, Cornet C and Bertru N 2019 Shape transition in InAs nanostructures formed by Stranski-Krastanow growth mode on InP (001) substrate *Appl. Phys. Lett.* **114** 173102

[12] Papatryfonos K, Rodary G, David C, Lelarge F, Ramdane A and Girard J-C 2015 One-dimensional nature of InAs/InP quantum dashes revealed by scanning tunneling spectroscopy *Nano Lett.* **15** 4488–97

[13] Gilfert C, Pavelescu E-M and Reithmaier J P 2010 Influence of the As2/As4 growth modes on the formation of quantum dot-like InAs islands grown on InAlGaAs/InP (100) *Appl. Phys. Lett.* **96** 191903

[14] Banyoudeh S and Reithmaier J P 2015 High-density 1.54μm InAs/InGaAlAs/InP(100) based quantum dots with reduced size inhomogeneity *J. Cryst. Growth* **425** 299–302

[15] Kim J S, Lee J H, Hong S U, Han W S, Kwack H-S and Oh D K 2003 Effects of a thin InGaAs layer on InAs quantum dots embedded in InAl(Ga)As *Appl. Phys. Lett.* **83** 3785–7

[16] Kim J S, Lee J H, Hong S U, Han W S, Kwack H-S, Lee C W and Oh D K 2003 Formation of self-assembled InAs quantum dots on InAl(Ga)As/InP and effects of a thin GaAs layer *J. Cryst. Growth* **259** 252–6

[17] Brault J, Gendry M, Grenet G, Hollinger G, Desières Y and Benyattou T 1998 Role of buffer surface morphology and alloying effects on the properties of InAs nanostructures grown on InP(001) *Appl. Phys. Lett.* **73** 2932–4

[18] González L, García J M, García R, Briones F, Martínez-Pastor J and Ballesteros C 2000 Influence of buffer-layer surface morphology on the self-organized growth of InAs on InP(001) nanostructures *Appl. Phys. Lett.* **76** 1104–6

[19] Wang B *et al* 2024 InAs quantum dots with a narrow photoluminescence linewidth for a lower threshold current density in 1.55 μm lasers *Opt. Mater. Express* **14** 1074–84

[20] Sercel P C 1995 Multiphonon-assisted tunneling through deep levels: a rapid energy-relaxation mechanism in nonideal quantum-dot heterostructures *Phys. Rev.* B **51** 14532–41

[21] Liao M, Li W, Tang M, Li A, Chen S, Seeds A and Liu H 2019 Selective area intermixing of III–V quantum-dot lasers grown on silicon with two wavelength lasing emissions *Semicond. Sci. Technol.* **34** 085004

[22] Li W, Chen S, Tang M, Wu J, Hogg R, Seeds A, Liu H and Ross I 2018 Effect of rapid thermal annealing on threading dislocation density in III–V epilayers monolithically grown on silicon *J. Appl. Phys.* **123** 215303

[23] Jiang W H, Xu H Z, Xu B, Ye X L, Wu J, Ding D, Liang J B and Wang Z G 2000 Annealing effect on the surface morphology and photoluminescence of InGaAs/GaAs quantum dots grown by molecular beam epitaxy *J. Cryst. Growth* **212** 356–9

[24] Yu Y, Fan G, Fermi A, Mazzaro R, Morandi V, Ceroni P, Smilgies D-M and Korgel B A 2017 Size-dependent photoluminescence efficiency of silicon nanocrystal quantum dots *J. Phys. Chem.* C **121** 23240–8

[25] Zhang Z Y, Jin P, Li Ch M, Ye X L, Meng X Q, Xu B, Liu F Q and Wang Z G 2003 The evolution of InAs/InAlAs/InGaAlAs quantum dots after rapid thermal annealing *J. Cryst. Growth* **253** 59–63

[26] Xu S J, Wang X C, Chua S J, Wang C H, Fan W J, Jiang J and Xie X G 1998 Effects of rapid thermal annealing on structure and luminescence of self-assembled InAs/GaAs quantum dots *Appl. Phys. Lett.* **72** 3335–7

[27] Bauer S, Sichkovskyi V, Schnabel F, Sengül A and Reithmaier J P 2019 Comparison between InP-based quantum dot lasers with and without tunnel injection quantum well and the impact of rapid thermal annealing *J. Cryst. Growth* **516** 34–39

[28] Babiński A, Jasiński J, Bożek R, Szepielow A and Baranowski J M 2001 Rapid thermal annealing of InAs/GaAs quantum dots under a GaAs proximity cap *Appl. Phys. Lett.* **79** 2576–8

[29] Djie H S, Wang Y, Ooi B S, Wang D-N, Hwang J C M, Dang G T and Chang W H 2006 Defect annealing of InAs–InAlGaAs quantum-dash-in-asymmetric-well laser *IEEE Photonics Technol. Lett.* **18** 2329–31

[30] Cao Q, Yoon S F, Tong C Z, Ngo C Y, Liu C Y, Wang R and Zhao H X 2009 Two-state competition in 1.3 μm multilayer InAs/InGaAs quantum dot lasers *Appl. Phys. Lett.* **95** 191101

[31] Zhao H, Yoon S F, Ngo C Y and Wang R 2011 Improved ground-state modulation characteristics in 1.3 μm InAs/GaAs quantum dot lasers by rapid thermal annealing *Nanoscale Res. Lett.* **6** 382

[32] Ahmed R *et al* 2007 Ab initio study of structural and electronic properties of III-arsenide binary compounds *Comput. Mater. Sci.* **39** 580–6

[33] Yeu I W, Han G, Park J, Hwang C S and Choi J-H 2019 Equilibrium crystal shape of GaAs and InAs considering surface vibration and new (111)B reconstruction: *ab-initio* thermodynamics *Sci. Rep.* **9** 1127

[34] Jiang M, Xiao H Y, Peng S M, Yang G X, Liu Z J and Zu X T 2018 A comparative study of low energy radiation response of AlAs, GaAs and GaAs/AlAs superlattice and the damage effects on their electronic structures *Sci. Rep.* **8** 2012

[35] Yu X, Jia H, Dear C, Yuan J, Deng H, Tang M and Liu H 2023 Optically enhanced single- and multi-stacked 1.55 μm InAs/InAlGaAs/InP quantum dots for laser applications *J. Phys. Appl. Phys.* **56** 285101

[36] Jung D, Ironside D J, Bank S R, Gossard A C and Bowers J E 2018 Effect of growth interruption in 1.55 μm InAs/InAlGaAs quantum dots on InP grown by molecular beam epitaxy *J. Appl. Phys.* **123** 205302

[37] Yuan J *et al* 2024 Indium-flush technique for C-band InAs/InP quantum dots *APL Mater.* **12** 121109

[38] Mtunzi M *et al* 2024 High-quality germanium growth on (111)-faceted V-groove silicon by molecular beam epitaxy *J. Phys. D: Appl. Phys.* **57** 255101

[39] Yang J, Jurczak P, Cui F, Li K, Tang M, Billiald L, Beanland R, Sanchez A M and Liu H 2019 Thin Ge buffer layer on silicon for integration of III–V on silicon *J. Cryst. Growth* **514** 109–13

[40] Chia C K, Chua S J, Tripathy S and Dong J R 2005 Group-V intermixing in InAs/InP quantum dots *Appl. Phys. Lett.* **86** 051905

[41] Kim J S, Kim E K, Park K, Yoon E, Han I K and Park Y J 2005 Effects of rapid thermal annealing on the energy levels of InAs/InP self-assembled quantum dots *Physica E Low Dimens. Syst. Nanostruct.* **26** 91–95

[42] Tripathy S, Chia C K, Dong J R and Chua S J 2005 Annealing-induced group V intermixing in InAs ⁄ InP quantum dots probed by Micro-Raman spectroscopy *Electrochem. Solid-State Lett.* **8** G194

[43] Wasilewski Z R, Fafard S and McCaffrey J P 1999 Size and shape engineering of vertically stacked self-assembled quantum dots *J. Cryst. Growth* **201–202** 1131–5

[44] Wei L, Da-Bing L, Zi-Yang Z, Chao-Rong L, Ze Z, Bo X and Zhan-Gum W 2005 Rapid thermal annealing effects on structural and optical properties of self-assembled InAs/GaAs quantum dots capped by InAlAs/InGaAs layers *Chin. Phys. Lett.* **22** 967

[45] Nellist P D 2019 Scanning transmission electron microscopy *Springer Handbook of Microscopy* ed P W Hawkes and J C H Spence (Springer International Publishing) pp 49–99

[46] Shi G X, Jin P, Xu B, Li C M, Cui C X, Wang Y L, Ye X L, Wu J and Wang Z G 2004 Thermal annealing effect on InAs/InGaAs quantum dots grown by atomic layer molecular beam epitaxy *J. Cryst. Growth* **269** 181–6

[47] Hÿtch M J, Snoeck E and Kilaas R 1998 Quantitative measurement of displacement and strain fields from HREM micrographs *Ultramicroscopy* **74** 131–46

[48] Fafard S and Allen C N 1999 Intermixing in quantum-dot ensembles with sharp adjustable shells *Appl. Phys. Lett.* **75** 2374–6

[49] Allen C N, Finnie P, Raymond S, Wasilewski Z R and Fafard S 2001 Inhomogeneous broadening in quantum dots with ternary aluminum alloys *Appl. Phys. Lett.* **79** 2701–3

[50] Barik S, Tan H H and Jagadish C 2007 High temperature rapid thermal annealing of phosphorous ion implanted InAs/InP quantum dots *Appl. Phys. Lett.* **90** 093106

[51] Deenapanray P N K, Tan H H, Fu L and Jagadish C 2000 Influence of low-temperature chemical vapor deposited SiO2 capping layer porosity on GaAs/AlGaAs quantum well intermixing *Electrochem. Solid-State Lett.* **3** 196

[52] Scott E G, Wake D, Spiller G D T and Davies G J 1989 Beryllium diffusion in GaInAs grown by molecular beam epitaxy *J. Appl. Phys.* **66** 5344–8

[53] Kim J S 2006 Self-assembled InAs quantum dots with two different matrix materials *J. Cryst. Growth* **290** 384–7

[54] Oh J W, Ryu M-Y, Jo B, Kim J S, Harris T R and Yeo Y K 2013 Bimodal luminescence behavior of spatially-ordered seven-stacked InAs/InAlGaAs quantum dots *Thin Solid Films* **541** 68–71

[55] Jones L, Yang H, Pennycook T J, Marshall M S J, Van Aert S, Browning N D, Castell M R and Nellist P D 2015 Smart Align—a new tool for robust non-rigid registration of scanning microscope data *Adv. Struct. Chem. Imaging* **1** 8

[56] Watanabe M, Okunishi E and Ishizuka K 2009 Analysis of spectrum-imaging datasets in atomic-resolution electron microscopy *Microsc. Anal.* **135**5

[57] Verbeeck J, Van Aert S and Bertoni G 2006 Model-based quantification of EELS spectra: including the fine structure *Ultramicroscopy* **106** 976–80

[58] HREM Research Inc. 2021 GPA for DigitalMicrograph (available at: www.hremresearch.com/gpa/)